HKIE THE HONG KONG INSTITUTION OF ENGINEERS 香港工程師學會

A novel hexagon-shaped interconnector for protonic ceramic electrolysis cells for large-scale green hydrogen production

Zheng Li and Meng Ni
Department of Building and Real Estate, Research Institute for Sustainable Urban Development (RISUD) and Research Institute for Smart Energy (RISE), The Hong Kong Polytechnic University, Hong Kong, People's Republic of China

ABSTRACT

Protonic ceramic electrolysis cells (PCECs) are the next generation of electrolysis technology for large-scale green hydrogen due to their lower power consumption but higher hydrogen production rate, compared with conventional alkaline electrolysis cells. The practical performance of PCEC stacks is still not satisfactory, and one key reason is the highly non-uniform distribution of H2O over large PCECs. To address the challenge of PCECs for practical application, a novel PCEC stack design with a hexagon-shaped interconnector is proposed and evaluated by using a comprehensive 3D numerical model. It is found that the novel interconnector can achieve higher uniformity indices for H2O and O2 by 11.7% and 46.2%, respectively. An overall performance index, integrating seven metrics, effectively identifies the hexagon-shaped interconnector with an 80 μm baffle thickness as the top performer. The methodology employed to derive this index proves to be a valuable tool for comprehensive performance evaluation, particularly in studies involving multiple metrics. This research lays a robust foundation for the optimisation of PCEC performance through an innovative interconnector design and advanced evaluation techniques.

KEYWORDS Protonic ceramic electrolysis cell; interconnector design; numerical modelling; faradaic efficiency; overall performance index; hydrogen production

CONTACT Zheng Li zldreamania@outlook.com

Received 3 March 2024

1. Introduction

The protonic ceramic electrolysis cell (PCEC) is a promising electrochemical device for realising large-scale green hydrogen production. Compared with the conventional alkaline electrolysis cell (AEC) and proton exchange membrane electrolysis cell (PEMEC), the PCEC shows the distinct features of a much lower power consumption but much higher rate of H_2 production. Thus, the PCEC is the next generation of electrolysis technology for green H_2 production. In this regard, the successful scale-up of the PCEC is of great importance to the development as well as the commercialisation of the PCEC.

The remarkable performance of a single PCEC has been experimentally proven and widely reported (Duan et al., 2019; Medvedev, 2019; Tarutin et al., 2020). However, in practical use, the interconnectors are applied to connect multiple single PCECs in series or parallel, which are finally assembled into a PCEC stack. In this regard, a PCEC stack can provide a much higher hydrogen production rate than a single PCEC under the same current density. However, compared with a single PCEC, due to the presence of the interconnector, the electrochemical performance of the PCEC stack is lower than a single PCEC (Timurkutluk et al., 2016). On the one hand, the gas distribution in the PCEC stack can be affected by the presence of interconnectors, thereby changing the concentration overpotential (Zeng et al., 2020). On the other hand, the interconnector can also affect the transfer route of electrons, therefore influencing the ohmic overpotential. Therefore, the interconnector is an important component of a PCEC stack. The convection design of the interconnector consisting of the straight gas channel and rectangular ribs is shown in Figure 1(a). Although the large area of contact between the ribs and the PEN facilitates the conduction of current, it inhibits the gas diffusion under the ribs, leading to an increase in the concentration overpotential. Therefore, some researchers have put a lot of effort into optimising conventional interconnector designs. Liu et al. (2009) developed a 3D model for solid oxide fuel cells (SOFC) to identify the optimal rib width under a given pitch width. It was found that under various flow configurations (co-flow, counter-flow, and cross-flow), the obtained optimal rib widths are very similar. A follow-up study conducted by Kong et al. (Kong et al., 2012) took the effects of the area-specific contact resistance (ASRcontact) on the optimal rib width into account. They identified the relationship between the optimal rib width, ASRcontact, and pitch width. Additionally, it was also found that the optimal rib width is different for different electrodes. Some works are not content with optimising designs. Some novel interconnector designs have been proposed to increase the contact area between the gas and the electrode surface. Li et al. (Li et al., 2005) proposed a discrete distributed column-type rib, which exhibited a better gas delivery performance than the conventional design. A discrete distributed X-type interconnector was proposed by Kong et al. (Kong et al., 2020). Simulation results demonstrated that the oxygen

concentration can be substantially improved by the new design, compared with the conventional interconnector. In addition, this new design was found to be superior to the traditional design under different porosities or conductivities of the anode and cathode. (Guo et al., 2022a; Guo et al., 2023) proposed six different discrete distributed interconnectors. It was found that the interconnector with staggered cuboid ribs showed the best performance when the ASRcontact was not considered. The results also indicated the rib size, its spatial distribution, ASRcontact, and the contact area between the interconnector and PEN were essential factors in the electrochemical performance of the cells. In addition to designing different discrete distributed interconnectors, some works have also proposed using other methods to enhance the transport of gas species into the porous electrodes. For example, (Chen et al., 2010; Chen et al., 2011) proposed a bi-layer interconnector design, in which the gas channels were not straight but contained the internal baffles formed by the double-layer interconnector. Simulation results suggested that this novel design enhanced the mass transfer. The concentration overpotential was reduced by nearly 5%. Fu et al. (Fu et al., 2021) modified the conventional design by adding fins in the gas channel, which can connect two ribs. This new design successfully interferes with the gas flow in the gas channel, enhancing the gas transport within the porous electrodes. Additionally, the results showed that this design can eliminate the zero-oxygen region and further reduce both activation and concentration overpotentials.

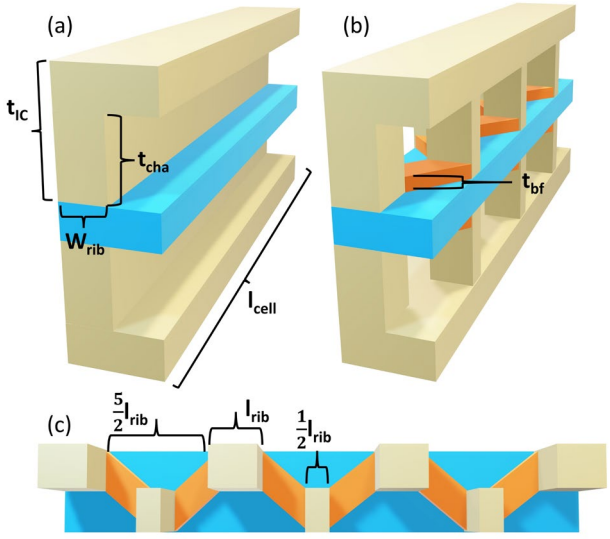

Figure 1. Schematics of (a) vertical cross-section of a PCEC with a conventional interconnector (blue represents the positive-electrode-electrolyte-negative electrode (PEN)); (b) vertical cross-section of a PCEC with the novel hexagon-shaped interconnector (yellow represents the ribs; orange represents the baffles connecting the discrete ribs) and (c) horizontal cross-section of a PCEC with the novel hexagon-shaped interconnector.

As mentioned above, for the design of the interconnector, the contact area between the gas channel and the porous electrode and the contact area between the interconnector and the porous electrode are both important. The former can provide enough area for the transport of gas, while the latter can offer enough contact for the transport of electrons. In this regard, a new interconnect design is proposed in this study (Figure 1[b]). The discretely distributed ribs ensure the mass transfer of gas. The baffles (Figure 1[c]) connecting the discrete ribs not only can ensure good connectivity for current transfer but also can disturb the gas transport. In order to quantify the effects of different interconnector designs on the electrochemical performance of a PCEC, the comparison between a PCEC using the conventional design and a PCEC using the new design is numerically performed. In the numerical model, only half of the repeating unit of the PCEC stack is considered in the computational domain (Figure 1[a] and [b]) to reduce the computational cost. Furthermore, to give a comprehensive understanding of this novel design, mass and momentum transfer, heat transfer, charge transfer, and the detailed electrochemistry are all taken into consideration in this model. Another important feature of this model is that the detailed charge transport within the electrolyte material is accounted for. Thus, the different designs of interconnectors can also be compared in terms of Faradaic efficiency. Furthermore, a uniformity index and a comprehensive performance index, which are based on an entropy weight method, are introduced to evaluate the uniformity of several local parameters' distribution as well as the overall performance of PCECs with different interconnectors. Therefore, this study can not only act as a guide for designing and evaluating novel interconnector designs for PCEC electrochemical performance but also as a guide for how to compare different interconnector designs.

2. Modelling methods

2.1. Modelling domain

The modelling domains of a PCEC using conventional design and novel design are respectively shown in Figure 1(a) and (b). Table 1 summarises the geometric parameters of 3D models as well as the other necessary input parameters adopted by the model. The assumptions applied in this model are listed as follows: (1) The gaseous species involved in the PCEC numerical model are considered ideal and incompressible; (2) Both the anode and cathode porous electrodes are fabricated with evenly distributed particles of both the electrolyte and electrode particles; (3) The microstructural properties of the electrode are assumed to follow the percolation theory; (4) The numerical model of the PCEC is under steady-state conditions; and (5) Only protons, electron holes, and oxygen vacancies are considered mobile in the electrolyte material.

2.2. Governing equations

As mentioned before, the 3D model takes various physical, chemical or electrochemical processes into consideration, including mass and momentum transfer, charge transfer in the electrolyte and electrode materials, heat transfer, electrochemistry as well as the defect chemistry. The governing equations used in constructing this numerical model are listed in Table 2. The dusty gas model (DGM) is implemented in this model to simulate gas diffusion in porous electrodes and flow channels. Darcy's term-modified Navier-Stokes equation is employed to describe the momentum transport in porous electrodes, while Darcy's term can be ignored in gas channels. The Butler-Volmer equation is applied to calculate the charge transfer reaction rate at the electrochemically active sites. The equilibrium potential is expressed by the Nernst equation. Note that the percolation theory is applied to obtain the microstructural properties of porous media. More details on the percolation theory can be found in (Chen et al., 2016, 2013, 2009). For describing the transfer of electrons in the electrode materials, Ohm's law is applied. Besides, the Nernst-Planck-Poisson (NPP) equation is used to simulate the transfer of different charge carriers in the electrolyte materials. The concentration of different charge carriers can be solved by defect chemistry.

2.3. Boundary conditions and model validation

The boundary conditions for the 3D models are as follows: (1) the operating pressure and working temperature are 1 atm and 600 °C, respectively; (2) a gas flow consisting of 80% H_2O and 20% air is introduced at the entrance of the anode gas channel, with a flow rate of 10 SCCM; (3) a gas flow consisting of 10% H_2O and 90% H_2 is introduced at the entrance of the cathode gas channel, with a flow rate of 4 SCCM; (4) open boundary conditions are applied at the exits of both the anode and cathode flow channels; (5) zero electrical potential is set to the outer face of the interconnector at the cathode side; (6) the current density is set to the outer face of the interconnector at the anode side; (7) the contact resistance is set to the interface between electrode and interconnector; and (8) the remaining boundaries are set as insulated walls or symmetries. The model validation is shown in Figure 2. A good agreement is achieved between the simulation results and experimental data (Tarutin et al., 2020). The 3D numerical model of the PCEC is built using the COMSOL platform based on the finite element method. The mesh of the model is fine enough to achieve mesh independence. The model takes approximately five hours to solve on a workstation with two 32-core CPUs and 256 GB of memory.

Table 1. Parameters of the 3D PCEC models (Chen et al., 2021; Duan et al., 2015; Guo et al., 2022b; Hinata et al., 2020; Wrubel et al., 2021).

Parameters	Value	Unit
t_{an}	30	μm
t_{ca}	400	μm
t_{ele}	15	μm
l_{cell}	30	mm
t_{cha}	1	mm
t_{IC}	0.5	mm
w_{rib}	0.5	mm
t_{bf}	80	μm
l_{rib}	3	mm
P_{op}	1	atm
T_{op}	600	°C
ε_{an}	0.4	1
ε_{ca}	0.4	1
$\tau_{an/ca}$	3	1
$r_{particle}$	0.5	μm
$V_{f,an}$	0.6	1
$V_{f,ca}$	0.6	1
Z	6	1
V_m	5.13×10^{-5}	$m^3\ mol^{-1}$

Table 2. List of governing equations used in the numerical model.

Descriptions	Equations	No.
Mass transport (Błesznowski et al., 2022; Brokaw, 1969; Jiang and Virkar, 2003)	$\frac{N_i}{D_{iK}^{eff}}+\sum_{j=1}^{n}\frac{y_jN_i-y_iN_j}{D_{ij}^{eff}}=-\frac{1}{RT}\left(P\nabla y_i+y_i\nabla P+y_i\nabla P\frac{kP}{D_{iK}^{eff}\mu}\right)$.	(1)
	$D_{iK}^{eff}=\frac{\varepsilon}{\tau}\frac{2}{3}r_p\sqrt{\frac{8RT}{\pi M_i}}$.	(2)
	$r_p=\frac{2}{3}\frac{\varepsilon}{1-\varepsilon}\frac{1}{V_{f,ed}/r_{ed}+V_{f,el}/r_{el}}$.	(3)
	$D_{ij}^{eff}=\frac{\varepsilon}{\tau}\cdot D_{ij}^{0}$.	(4)
	$D_{ij}^{0}=\frac{0.042851\times\left(\frac{1}{M_i}+\frac{1}{M_j}\right)^{-0.5}-0.0098\times T^{1.5}}{P\Omega_D\sigma_{ij}^2}$.	(5)
Momentum transport (Li et al., 2022a; Xu et al., 2021)	$\frac{\rho}{\varepsilon}(\boldsymbol{u}\cdot\nabla)\cdot\frac{\boldsymbol{u}}{\varepsilon}=-\nabla P+\nabla\cdot\left[\frac{\mu}{\varepsilon}(\nabla\boldsymbol{u}+\nabla\boldsymbol{u}^T)-\frac{2}{3}\frac{\mu}{\varepsilon}(\nabla\cdot\boldsymbol{u})\right]-\left(\mu\kappa^{-1}+\frac{Q_m}{\varepsilon^2}\right)\boldsymbol{u}$.	(6)
	$\rho\nabla\cdot\boldsymbol{u}=Q_m=\sum y_i R_i$.	(7)
	$\rho=\frac{P}{RT}\sum_i\frac{\omega_i}{M_i}$.	(8)
Heat transport (Li et al., 2022b)	$\rho C_{p,eff}\boldsymbol{u}\nabla T+\nabla\cdot\left(-\lambda_{eff}\nabla T\right)=Q_h$.	(9)
Charge transfer reaction rate	$i=i_0[\exp\left(\frac{\alpha F\eta_{act}}{RT}\right)-\exp\left(\frac{-(1-\alpha)F\eta_{act}}{RT}\right)]$.	(10)
Equilibrium potential	$E_{eq}=-\frac{\Delta G^0}{2F}+\frac{RT}{2F}\ln\left(\frac{p_{H2}^l(p_{O2}^l)^{0.5}}{p_{H2O}^l}\right)$.	(11)
Exchange current density (Luo et al., 2019)	$i_{0,a}=\gamma_{0,a}\exp\left(-\frac{E_{act,a}}{RT}\right)[OH_0]^{\beta_a}[O_0^{\times}]^{1-\beta_a}p_{O_2}^{0.25}p_{H_2O}$.	(12)
	$i_{0,c}=\gamma_{0,c}\exp\left(-\frac{E_{act,c}}{RT}\right)[OH_0]^{\beta_c}[O_0^{\times}]^{1-\beta_c}p_{H_2}$.	(13)
Current source (Costamagna et al., 1998)	$S_i=\lambda_{TPB}^{eff}\cdot i$.	(14)
	$\lambda_{TPB}^{eff}=2\pi\min(r_{ed},r_{el})^2P_{per,ed}P_{per,el}\sin(\theta/2)n_{ed}^v$.	(15)
	$n_{ed}^v=(1-\varepsilon)V_{f,ed}/(\frac{4}{3}\pi r_{ed}^3)$.	(16)
	$P_{per}=1-\left[\left((4.236-Z_{k,k})/2.472\right)^{2.5}\right]^{0.4}$.	(17)
	$Z_{k,k}=Z\frac{V_{f,k}/r_k}{V_{f,k}/r_k+V_{f,p}/r_p}$.	(18)
Charge transport (Euser et al., 2016; Li et al., 2020)	$J_i=-D_i^{eff}\left(\nabla c_i+\frac{z_iF}{RT}c_i\nabla\phi_{el}\right)$.	(19)
Charge carriers' conservation	$\frac{\partial c_i}{\partial t}+\nabla\cdot J_i=s_d$.	(20)
Electrostatic potential (Peters, 2009)	$\nabla\cdot(\varepsilon_{abs}\nabla\phi_{el})+F\sum_i z_ic_i=0$.	(21)
External current density	$i_{ex}=F\sum_i z_iJ_i=\sum_i i_i=\sum_i z_iFJ_i$.	(22)
Electrolyte conductivity (Zhu et al., 2018)	$\sigma_{el}=\sum_i\frac{F^2}{RT}z_i^2c_iD_i$.	(23)
	$\sigma_i=\frac{F^2}{RT}z_i^2c_iD_i$.	(24)
	$D_i=D^0\exp\left(-E_{act,d}/RT\right)$.	(25)
Electronic charge conservation (Beale et al., 2021)	$\nabla\cdot\boldsymbol{i}_e=\nabla\cdot(\sigma_{e,eff}\nabla\phi_e)$.	(26)
	$\sigma_{eff}=\sigma_0\left[(1-\varepsilon)V_fP_{per}\right]^{\zeta}$.	(27)
Contact resistance (Liu et al., 2008; Russner et al., 2020)	$i_{local}=\Delta\phi_{cross}/ASR_{contact}$.	(28)
	$ASR_{contact}=17119\exp\left(-0012T[1/K]\right)$.	(29)

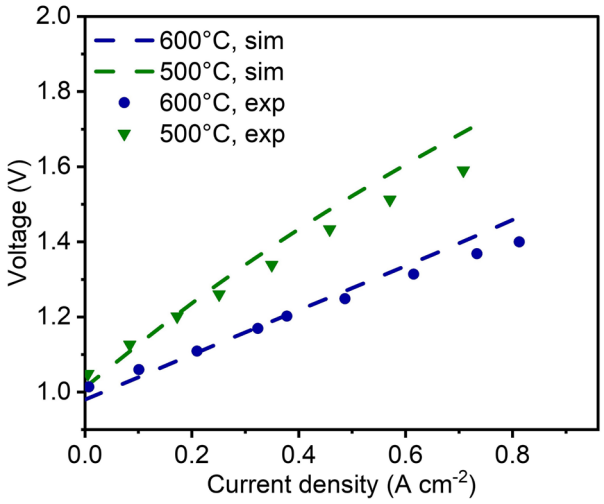

Figure 2. The model validation.

3. Results and discussion

3.1. Consideration of contact resistance

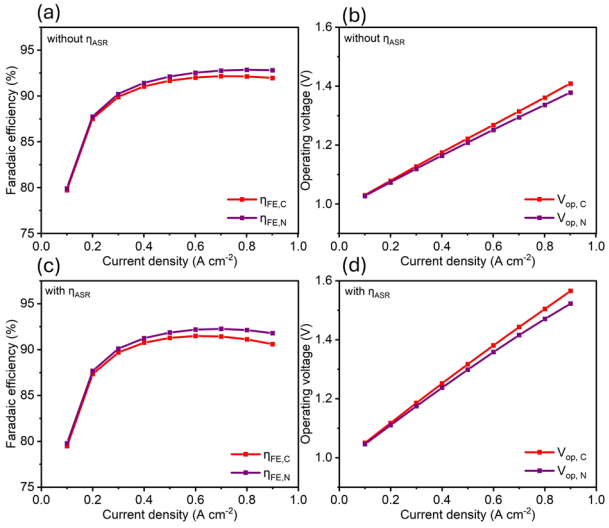

Figure 3. (a) Faradaic efficiency comparison without the consideration of the contact resistance; (b) operating voltage comparison without the consideration of the contact resistance; (c) Faradaic efficiency comparison with the consideration of the contact resistance; and (d) operating voltage comparison with the consideration of the contact resistance.

Figure 3 shows the difference in electrochemical performance/Faradaic efficiency (FE) with and without the contact resistance. It is evident that both the FE and electrochemical performance of the two designs decline when considering the contact resistance. For instance, at a current density of 0.8 A cm-2 in the conventional design, accounting for the contact resistance results in a

5.3% decrease in FE, coupled with a 12.7% increase in operating voltage. This highlights the significant impact of considering the contact resistance on the prediction of electrochemical performance and FE in PCECs, emphasising the necessity to account for it in the simulation. Without accounting for the contact resistance, the novel hexagon-shaped design shows a 1.1% higher FE and a 2.3% lower operating voltage compared to the conventional design. When the contact resistance is considered, the novel design still exhibits a 1.2% higher FE and a 3% lower operating voltage than the conventional design. This observation indicates that accounting for the contact resistance also leads to a slight increase in the performance difference between the two designs. Therefore, in the subsequent case studies, the contact resistance is considered to provide a more realistic simulation.

3.2. Case studies

It is worth noting that this study investigated a total of four cases, which are listed in Table 3. In addition, to quantitatively evaluate the uniformity of the distributions of various local parameters (p) in the PCEC, the uniformity index is introduced as (Li et al., 2022b):

$$\Gamma_p = 1 - \left(\frac{\sum_{i=1}^{n} [\frac{p_i - \bar{p}}{\bar{p}}]^2}{n} \right)^{0.5}, \quad (30)$$

where Γ_p denotes the uniformity index of the local parameter p; $\bar{p}$ is the mean value of p while the p_i stands for the local value.

Table 3. The four cases.

Cases	Descriptions	Remarks
1 (Base)	Conventional design	None
2		$t_{bf} = 80\ \mu m$
3	New design	$t_{bf} = 65\ \mu m$
4		$t_{bf} = 50\ \mu m$

3.2.1. Electrochemical performance and pressure drop

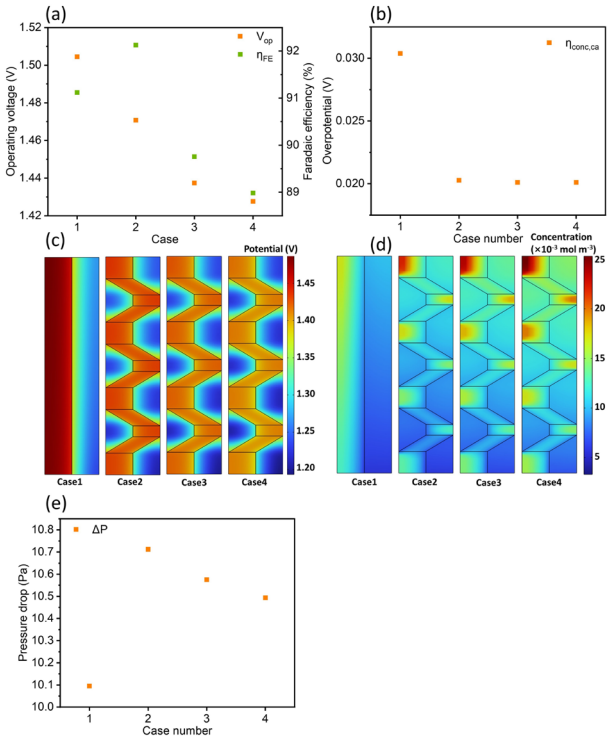

Figure 4. (a) Electrochemical performance and FE comparison; (b) concentration overpotential comparison; (c) distribution of electric potential at the anode side; (d) concentration distribution of electronic holes at the anode side; and (e) pressure drop.

As shown in Figure 4(a), the novel design outperforms the conventional design in terms of electrochemical performance. Additionally, a notable observation is that a reduction in baffle thickness corresponds to a decrease in both overpotential and FE. The concentration overpotential of the different cases is detailed in Figure 4(b), revealing a significant decrease in concentration loss due to the presence of baffles. In addition, as depicted in Figure 4(c), the contact resistance leads to a substantial high ohmic loss in the PCECs. This ohmic loss decreases with reduced baffle thickness. Consequently, the combined effect of reduced concentration and ohmic overpotentials contributes to a superior electrochemical performance in the novel design. The decrease in FE with the decreasing baffle thickness can be explained by Figure 4(d). As the baffle thickness decreases, the concentration of electronic holes increases gradually, leading to a reduction in FE. Furthermore, the electronic holes tend to concentrate under the rib region, which indicates that the distribution of gas in the electrode can significantly affect the distribution of charge carriers. It is noteworthy that the introduction of baffles leads to an increase in pressure drop within the PCECs (Figure 4(e)).

3.2.2. Chemical species distribution

In Figure 5(a) and (b), two uniformity indices are notably higher in the novel design compared to the conventional design. For example, the uniformity indices of H_2O and O_2 of Case 2 are 11.7% and 46.2% higher, respectively, than those of Case 1. This observation underscores that the novel hexagon-shaped design can markedly enhance the gas distribution on the anode side, particularly for oxygen. Moreover, it is reasonable to project that this novel design may also prove effective in the fuel cell mode, as it substantially improves the distribution of oxygen, a reactant gas in the fuel cell mode. Furthermore, two uniformity indices slightly increase as the baffle thickness decreases. The distribution of the steam mole fraction in the anode of different cases is shown in Figure 5(c). In comparison to the conventional design, the novel hexagon-shaped design exhibits a significantly lower area with a steam fraction of less than 0.2. This highlights the favourable impact of the novel interconnector on achieving an even distribution of steam. However, it is notable that the mole fraction of steam under the rib in the novel design remains much lower than that under the channel. Consequently, to optimise the hexagon-shaped interconnector design, further research can explore the size and shape of discretely distributed ribs and their influence on gas species distribution, as well as the electrochemical performance of PCECs. Additionally, the application of the novel design also has a slightly positive impact on hydrogen distribution in the cathode. In Figure 5(d), the uniformity index of Case 2 is 0.45% higher than of Case 1.

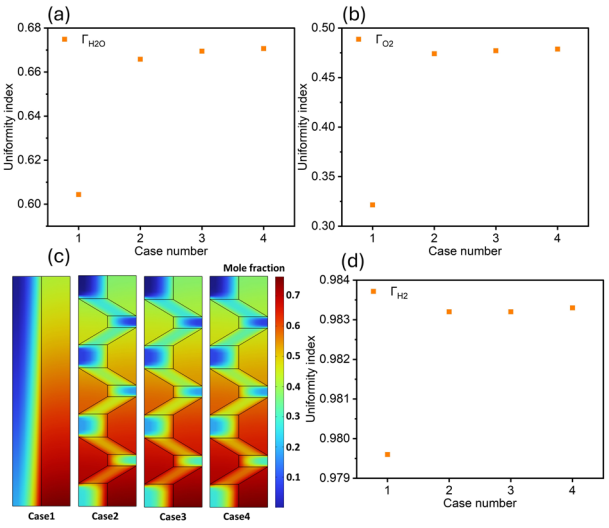

Figure 5. (a) Uniformity index of H_2O distribution; (b) uniformity index of O_2 distribution; (c) the distribution of steam fraction in the anode; and (d) uniformity index of H_2 distribution.

3.2.3. Performance index

In this study, a comprehensive performance index is introduced to assess the overall performance of various cases, considering multiple performance metrics. These metrics encompass pressure drop, Faradaic efficiency (FE), operating voltage, and uniformity indices of steam, temperature, FE, and current density. The formulation of the overall performance index is outlined as follows (Wang et al., 2023):

(1) Standardise all the performance metrics, where i is the index of cases, j is the index of performance metrices, a_{ij} is the jth metrix of case ith, $\max_j a_{ij}$ is the maximum value of the jth metrics, $\min_j a_{ij}$ is the minimum value of the jth metrics.

$$a_{ij}^s = \frac{a_{ij} - \min_j a_{ij}}{\max_j a_{ij} - \min_j a_{ij}} . \tag{31}$$

(2) Calculate the coefficient of weight for the jth metric, w_j, where e_j is the coefficient of entropy, g_j is the coefficient of variation, p_{ij} is the averaged performance metrics.

$$w_j = \frac{g_j}{\sum_{j=1}^{n} g_j} , \tag{32}$$

$$g_j = 1 - e_j = 1 + \frac{\sum_{i=1}^{m} p_{ij} \ln (p_{ij})}{\ln (m)} , \tag{33}$$

$$p_{ij} = \frac{a_{ij}^s}{\sum_{i=1}^{m} a_{ij}^s} . \tag{34}$$

(3) Compute the overall performance index, E_i.

$$E_i = \sum_{j=1}^{n} w_j p_{ij} . \tag{35}$$

The calculated overall performance indices are illustrated in Figure 6. The figure suggests that Case 2 is identified as the best case because its overall performance index is 70% higher than that of the conventional case and 42% higher than that of Case 3 or Case 4. This indicates that a novel hexagon-shaped interconnector with an 80 μm baffle outperforms the other cases significantly in terms of the overall performance index.

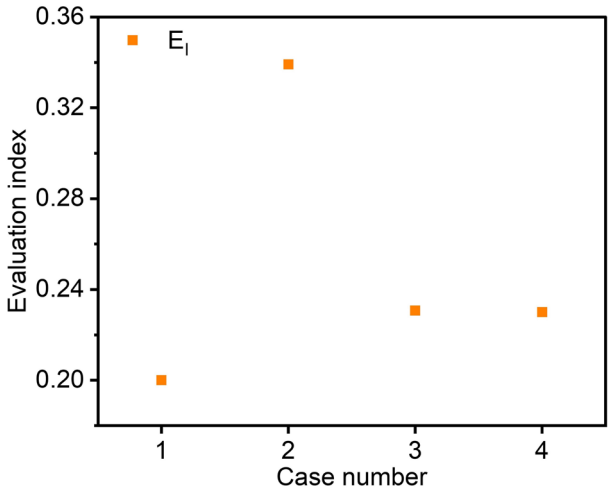

Figure 6. Overall performance index.

4. Conclusion

In this study, a novel hexagon-shaped interconnector is introduced with the aim of enhancing the anode performance of PCECs, consequently improving their hydrogen production capability. To assess the effectiveness of this design, a 3D numerical model is developed, which couples mass, momentum, charge, and energy transfer with electrochemistry sub-models. This comprehensive model is employed to evaluate the performance of PCECs featuring the novel interconnector design.

The simulation results underscore the notable influence of the contact resistance on the electrochemical performance and FE. To provide a more realistic prediction, it is crucial to consider the contact resistance in the model geometry, especially in the presence of the interconnector. Generally, the novel hexagon-shaped interconnector demonstrates superior electrochemical performance and FE. Additionally, the novel design significantly affects the distribution of gas on both the anode and cathode sides, as highlighted by the substantially enhanced uniformity indices. In this study, an overall performance index is introduced to assess and compare the performance of different cases featuring various designs. Seven performance metrics are averaged based on their coefficients of entropy to formulate the overall performance index. The results identify the novel hexagon-shaped interconnector with a baffle thickness of 80 μm as the best-performing case.

Overall, the novel hexagon-shaped interconnector proposed in this study exhibits significant advantages over the traditional interconnector. The developed 3D model can be extended to evaluate the performance of other interconnector designs. Future work may focus on exploring the size and shape of discretely distributed ribs in the hexagon-shaped interconnector to further optimise its performance. Additionally, the method used to derive the overall performance index can serve as a valuable tool in other studies aiming to evaluate comprehensive performance, especially when dealing with numerous performance metrics.

Acknowledgments

Meng Ni thanks the grant (Project Number: 15306723) from the Research Grants Council, University Grants Committee, Hong Kong SAR.

Notes on contributors

Mr Li Zheng is now a Ph.D. student of the Department of Building and Real Estate at The Hong Kong Polytechnic University. His research interests include multi-physical modelling of electrolysers, machine learning-based surrogate models of electrolysers, and Artificial intelligence (AI) applications in electrochemical reactors.

Prof Meng Ni received his Ph.D. from The University of Hong Kong. Currently, he is a Professor and Associate Dean (Faculty of Construction and Environment) at The Hong Kong Polytechnic University. His research interests include fuel cells, rechargeable batteries and electrochemical systems for low-grade heat utilisation. Prof Ni is a Senior Editor for Sustainable Energy Technologies and Assessments (Elsevier) and an Associate Editor for two other journals. He is an active reviewer for over 80 academic journals.

Financial interest disclosure statement

The authors declare that they have no known competing financial interests or personal relationships that could have appeared to influence the work reported in this paper.

References

[1] Beale SB, Andersson M, Boigues-Muñoz C, Frandsen HL, Lin Z, McPhail SJ, Ni M, Sundén B, Weber A and Weber AZ (2021). Continuum scale modelling and complementary experimentation of solid oxide cells. *Progress in Energy and Combustion Science*, 85, pp. 100902. https://doi.org/10.1016/j.pecs.2020.100902

[2] Błesznowski M, Sikora M, Kupecki J, Makowski Ł and Orciuch W (2022). Mathematical approaches to modelling the mass transfer process in solid oxide fuel cell anode. *Energy*, 239, pp. 121878. https://doi.org/10.1016/j.energy.2021.121878

[3] Brokaw RS (1969). Predicting Transport Properties of Dilute Gases. *Industrial & Engineering Chemistry Process Design and Development*, 8, pp. 240–253. https://doi.org/10.1021/i260030a015

[4] Chen D, He H, Zhang D, Wang H and Ni M (2013). Percolation Theory in Solid Oxide Fuel Cell Composite Electrodes with a Mixed Electronic and Ionic Conductor. *Energies*, 6, pp. 1632–1656. https://doi.org/10.3390/en6031632

[5] Chen D, Lin Z, Zhu H and Kee RJ (2009). Percolation theory to predict effective properties of solid oxide fuel-cell composite electrodes. *Journal of Power Sources*, 191, pp. 240–252. https://doi.org/10.1016/j.jpowsour.2009.02.051

[6] Chen D, Zhang Q, Lu L, Periasamy V, Tade MO and Shao Z (2016). Multi scale and physics models for intermediate and low temperatures H+-solid oxide fuel cells with H+/e−/O2− mixed conducting properties: Part A, generalized percolation theory for LSCF-SDC-BZCY 3-component cathodes. *Journal of Power Sources*, 303, pp. 305–316. https://doi.org/10.1016/j.jpowsour.2015.10.090

[7] Chen Q, Wang Q, Zhang J and Yuan J (2011). Effect of bi-layer interconnector design on mass transfer performance in porous anode of solid oxide fuel cells. *International Journal of Heat and Mass Transfer*, 54, pp. 1994–2003. https://doi.org/10.1016/j.ijheatmasstransfer.2011.01.003

[8] Chen Q, Zeng M, Zhang J and Wang Q (2010). Optimal design of bi-layer interconnector for SOFC based on CFD-Taguchi method. *International Journal of Hydrogen Energy*, 35, 4292–4300. https://doi.org/10.1016/j.ijhydene.2010.01.117

[9] Chen T, Jing Y, Anderson LO, Leonard K, Matsumoto H, Aluru N and Perry NH (2021). Toward Durable Protonic Ceramic Cells: Hydration-Induced Chemical Expansion Correlates with Symmetry in the Y-Doped BaZrO3–BaCeO3 Solid Solution. *The Journal of Physical Chemistry C*, 125, pp. 26216–26228. https://doi.org/10.1021/acs.jpcc.1c08334

[10] Costamagna P, Costa P and Antonucci V (1998). Micro-modelling of solid oxide fuel cell electrodes. *Electrochimica Acta*, 43, pp. 375–394. https://doi.org/10.1016/S0013-4686(97)00063-7

[11] Duan C, Kee R, Zhu H, Sullivan N, Zhu L, Bian L, Jennings D and O'Hayre R (2019). Highly efficient reversible protonic ceramic electrochemical cells for power generation and fuel production. *Nature Energy*, 4, pp. 230–240. https://doi.org/10.1038/s41560-019-0333-2

[12] Duan C, Tong J, Shang M, Nikodemski S, Sanders M, Ricote S, Almansoori A and O'Hayre R, (2015). Readily processed protonic ceramic fuel cells with high performance at low temperatures. *Science*, 349, pp. 1321–1326. https://doi.org/10.1126/science.aab3987

[13] Euser B, Berger JR, Zhu H and Kee RJ (2016). Defect-Transport-Induced Stress in Mixed Ionic-Electronic Conducting (MIEC) Ceramic Membranes. *Journal of The Electrochemical Society*, 163(3), pp. F264. https://doi.org/10.1149/2.1021603jes

[14] Fu Q, Li Z, Wei W, Liu F, Xu X and Liu Z (2021). Performance enhancement of planar solid oxide fuel cell using a novel interconnector design. *International Journal of Hydrogen Energy*, 46(41), pp. 21634–21656. https://doi.org/10.1016/j.ijhydene.2021.04.001

[15] Guo M, He Q, Cheng C, Zhao D and Ni M (2022a). New interconnector designs for electrical performance enhancement of solid oxide fuel cells: A 3D modelling study. *Journal of Power Sources*, 533, 231373. https://doi.org/10.1016/j.jpowsour.2022.231373

[16] Guo M, Ru X, Yang L, Ni M and Lin Z (2022b). Effects of methane steam reforming on the mechanical stability of solid oxide fuel cell stack. *Applied Energy*, 322, pp. 119464. https://doi.org/10.1016/j.apenergy.2022.119464

[17] Guo M, Zhao D, Xu Q, Li Z, Xu H and Ni M (2023). New interconnector design optimization to balance electrical and mechanical performance of solid oxide fuel cell stack. *International Journal of Hydrogen Energy*, 48, pp. 3107–3121. https://doi.org/10.1016/j.ijhydene.2022.10.147

[18] Hinata K, Sata N, Costa R and Iguchi F (2020). High Temperature Elastic Modulus of Proton Conducting Ceramics Y-Doped Ba(Zr,Ce)O3. *ECS Meeting Abstracts*, MA2020-02, pp. 2617–2617. https://doi.org/10.1149/MA2020-02402617mtgabs

[19] Jiang Y and Virkar AV (2003). Fuel Composition and Diluent Effect on Gas Transport and Performance of Anode-Supported SOFCs. *Journal of The Electrochemical Society*, 150, A942. https://doi.org/10.1149/1.1579480

[20] Kong W, Han Z, Lu S, Gao X and Wang X (2020). A novel interconnector design of SOFC. International Journal of Hydrogen Energy, The 7th International Conference on Energy, *Engineering and Environmental Engineering*, 45, pp. 20329–20338. https://doi.org/10.1016/j.ijhydene.2019.10.252

[21] Kong W, Li J, Liu S and Lin Z (2012). The influence of interconnect ribs on the performance of planar solid oxide fuel cell and formulae for optimal rib sizes. *Journal of Power Sources*, 204, pp. 106–115. https://doi.org/10.1016/j.jpowsour.2012.01.041

[22] Li K, Araki T, Kawamura T, Ota A and Okuyama Y (2020). Numerical analysis of current efficiency distributions in a protonic ceramic fuel cell using Nernst-Planck-Poisson model. *International Journal of Hydrogen Energy*, 45, pp. 34139–34149. https://doi.org/10.1016/j.ijhydene.2020.09.143

[23] Li PW, Chen SP and Chyu MK (2005). To Achieve the Best Performance Through Optimization of Gas Delivery and Current Collection in Solid Oxide Fuel Cells. Journal of Fuel Cell Science and Technology, 3, pp. 188–194. https://doi.org/10.1115/1.2174068

[24] Li Z, He Q, Wang C, Xu Q, Guo M, Bello IT and Ni M (2022a). Ethylene and power cogeneration from proton ceramic fuel cells (PCFC): A thermo-electrochemical modelling study. *Journal of Power Sources*, 536, pp. 231503. https://doi.org/10.1016/j.jpowsour.2022.231503

[25] Li Z, He Q, Xia L, Xu Q, Cheng C, Wang J and Ni M (2022b). Effects of cathode thickness and microstructural properties on the performance of protonic ceramic fuel cell (PCFC): A 3D modelling study. *International Journal of Hydrogen Energy*, 47, pp. 4047–4061. https://doi.org/10.1016/j.ijhydene.2021.11.022

[26] Liu S, Kong W and Lin Z (2009). Three-dimensional modeling of planar solid oxide fuel cells and the rib design optimization. *Journal of Power Sources*, 194, pp. 854–863. https://doi.org/10.1016/j.jpowsour.2009.06.056

[27] Liu S, Song C and Lin Z (2008). The effects of the interconnect rib contact resistance on the performance of planar solid oxide fuel cell stack and the rib design optimization. *Journal of Power Sources*, 183, pp. 214–225. https://doi.org/10.1016/j.jpowsour.2008.04.054

[28] Luo Y, Shi Y, Liao S, Chen C, Zhan Y, Au C-T and Jiang L (2019). Coupling ammonia catalytic decomposition and electrochemical oxidation for solid oxide fuel cells: A model based on elementary reaction kinetics. *Journal of Power Sources*, 423, pp. 125–136. https://doi.org/10.1016/j.jpowsour.2019.03.064

[29] Medvedev D (2019). Trends in research and development of protonic ceramic electrolysis cells. *International Journal of Hydrogen Energy*, 44, pp. 26711–26740. https://doi.org/10.1016/j.ijhydene.2019.08.130

[30] Peters C (2009). *Grain-size Effects in Nanoscaled Electrolyte and Cathode Thin Films for Solid Oxide Fuel Cells (SOFC)*. KIT Scientific Publishing.

[31] Russner N, Dierickx S, Weber A, Reimert R and Ivers-Tiffée E (2020). Multiphysical modelling of planar solid oxide fuel cell stack layers. *Journal of Power Sources*, 451, pp. 227552. https://doi.org/10.1016/j.jpowsour.2019.227552

[32] Tarutin A, Kasyanova A, Lyagaeva J, Vdovin G and Medvedev D (2020). Towards high-performance tubular-type protonic ceramic electrolysis cells with all-Ni-based functional electrodes. *Journal of Energy Chemistry*, 40, pp. 65–74. https://doi.org/10.1016/j.jechem.2019.02.014

[33] Timurkutluk B, Timurkutluk C, Mat MD and Kaplan Y (2016). A review on cell/stack designs for high performance solid oxide fuel cells. *Renewable and Sustainable Energy Reviews*, 56, pp. 1101–1121. https://doi.org/10.1016/j.rser.2015.12.034

[34] Wang Y, Guan C, Li H, Zhao Y, Wang C and He W (2023). Flow field configuration design for a large-scale hydrogen polymer electrolyte membrane fuel cell. *Applied Energy*, 351, pp. 121852. https://doi.org/10.1016/j.apenergy.2023.121852

[35] Wrubel JA, Gifford J, Ma Z, Ding H, Ding D and Zhu T (2021). Modeling the performance and faradaic efficiency of solid oxide electrolysis cells using doped barium zirconate perovskite electrolytes. *International Journal of Hydrogen Energy*, 46, pp. 11511–11522. https://doi.org/10.1016/j.ijhydene.2021.01.043

[36] Xu Q, Xia L, He Q, Guo Z and Ni M (2021). Thermo-electrochemical modelling of high temperature methanol-fuelled solid oxide fuel cells. *Applied Energy*, 291, pp. 116832. https://doi.org/10.1016/j.apenergy.2021.116832

[37] Zeng Z, Qian Y, Zhang Y, Hao C, Dan D and Zhuge W (2020). A review of heat transfer and thermal management methods for temperature gradient reduction in solid oxide fuel cell (SOFC) stacks. *Applied Energy*, 280, pp. 115899. https://doi.org/10.1016/j.apenergy.2020.115899

[38] Zhu H, Ricote S, Duan C, O'Hayre RP, Tsvetkov DS and Kee RJ (2018). Defect Incorporation and Transport within Dense BaZr0.8Y0.2O3−δ (BZY20) Proton-Conducting Membranes. *Journal of The Electrochemical Society*, 165, pp. F581. https://doi.org/10.1149/2.0161809jes

Appendix

Nomenclature

Abbreviations

PCEC	Protonic ceramic electrolysis cell
SOFC	Solid oxide fuel cell
NPP	Nernst-Planck-Poisson

Letter

T	Absolute temperature, K
E_{act}	Activation energy, J mol^{-1}
R	Universal molar gas constant, 8.314 J mol^{-1} k^{-1}
E_{eq}	Equilibrium potential, V
c_i	Concentration, mol m^{-3}
J_i	Molar flux, mol m^{-2} s^{-1}
F	Faraday constant, 96485.3 C mol^{-1}
z_i	Number of charges
ϕ_{el}	Electrostatic potential, V
i	Current density, A m^{-2}
y_i	Molar fraction of species i, mol s^{-1}
V_f	Volume fraction
P_{per}	Percolation probability
λ_{TPB}^{eff}	Effective TPB, m^2 m^{-3}
M_i	Molar mass of species i, kg mol^{-1}
u	Velocity, m s^{-1}
N_i	Molar flux of species I, mol m^{-2} s^{-1}
D_{iK}^{eff}	Effective Knudsen diffusion coefficient of species i, m^2 s^{-1}
D_{ij}^{eff}	Effective binary diffusion coefficient, m^2 s^{-1}
C_p	Thermal capacity, J mol^{-1} k^{-1}
λ_{eff}	Effective thermal conductivity, W m^{-1} k^{-1}
Q_i	Source term i
ρ	Density, kg m^{-3}
σ	Conductivity, S m^{-1}
ε	Porosity
τ	Tortuosity
k	Permeability, m^2
ω_i	Mass fraction of species i
μ	Viscosity, Pa s